Materials Advances

ROYAL SOCIETY OF CHEMISTRY

PAPER

View Article Online
View Journal | View Issue

Cite this: *Mater. Adv.*, 2022, 3, 8229

Ambient-pressure ozone treatment enables tuning of oxygen vacancy concentration in the $La_{1-x}Sr_xFeO_{3-\delta}$ ($0 \leq x \leq 1$) perovskite oxides†

Geletu Qing,[a] David Thompson,[a] Mourad Benamara,[b] Clemens Heske,[cd] Lauren Greenlee*[e] and Jingyi Chen*[a]

Oxygen vacancies in metal oxides can determine their properties. However, it is difficult to reduce the oxygen vacancy concentration in metal oxides without annealing them under high pressure. In this work, we develop a facile approach to control oxygen vacancy content *via* an ozone treatment under ambient pressure during cooling. This approach is demonstrated for the synthesis of $La_{1-x}Sr_xFeO_{3-\delta}$ ($0 \leq x \leq 1$, $0 \leq \delta \leq 0.5x$) perovskite oxides – an important class of energy-related materials due to their wide range of non-stoichiometry, mixed ionic and electronic conductivity, and the presence of a rare Fe(IV) oxidation state. A series of $La_{1-x}Sr_xFeO_{3-\delta}$ compounds was initially synthesized using a polymerized complex method. The concentration of oxygen vacancies and Fe(IV) were determined by redox titration, and the crystal structures were derived by analyzing X-ray diffraction patterns using Rietveld refinement. Significant amounts of oxygen vacancies were found in the as-synthesized compounds with $x \geq 0.8$: $La_{0.2}Sr_{0.8}FeO_{3-\delta}$ ($\delta = 0.066$) and $SrFeO_{3-\delta}$ ($\delta = 0.195$). The ambient-pressure ozone treatment approach was able to substantially reduce the amount of oxygen vacancies in these compounds to achieve levels near the oxygen stoichiometry of 3 for $La_{0.2}Sr_{0.8}FeO_{3-\delta}$ ($\delta = 0.006$) and $SrFeO_{3-\delta}$ ($\delta = 0.021$). The oxygenation/deoxygenation kinetics can be tuned by the cooling rate after annealing. As the oxygen vacancy concentration decreases, the structure of $SrFeO_{3-\delta}$ evolves from orthorhombic to cubic, demonstrating that the crystal structures in metal oxides can be highly sensitive to the number of oxygen vacancies. The ozone treatment approach developed in this study may thus offer a robust means to tune the properties of a wide variety of metal oxides.

Received 28th May 2022,
Accepted 5th September 2022

DOI: 10.1039/d2ma00604a

rsc.li/materials-advances

1. Introduction

Oxygen vacancies have a profound effect on both bulk (*e.g.*, ionic/electronic conductivity and optical properties) and surface properties (*e.g.*, catalytic activity) of transition metal oxides.[1–3] Changes in oxygen stoichiometry alter the surface electronic structure of metal oxides and thus affect the adsorption strength of reactants and intermediates on the surface, which is critical for surface-catalyzed reactions. A number of studies have demonstrated that catalytic activity varies with the concentration of oxygen vacancies in the transition metal oxides, including materials such as Co_3O_4, $Ca_2Mn_2O_5$, $SrCoO_x$, and MnO_2 in oxygen evolution/reduction,[4–7] SnO_x and ZnO in carbon dioxide reduction,[8,9] and $La_xSrO_{3-\delta}$ and Cr-doped CeO_2 in nitrogen reduction,[10,11] as well as CeO_2, MnO, and $Li[Li_{0.144}Ni_{0.136}Co_{0.136}Mn_{0.544}]O_2$ in battery application.[12–14] The oxygen vacancies can also affect other applications of oxides and their hybrids, such as electromagnetic wave absorption.[15–18] However, a versatile strategy of controlling the oxygen vacancy in metal oxides remains lacking. Hence, this work focuses on method development of tuning the oxygen vacancy density of metal oxides, in particular perovskite oxides such as $La_{1-x}Sr_xFeO_{3-\delta}$ ($0 \leq x \leq 1$, $0 \leq \delta \leq 0.5x$), which are known to have a wide range of non-stoichiometry.

The $La_{1-x}Sr_xFeO_{3-\delta}$ perovskites are also known to be one of the few compound suites that contain Fe(IV), where the substitution of La(III) with Sr(II) results in the oxidation of Fe(III) to Fe(IV); however, oxygen vacancies would also tend to compensate for the decrease in positive electric charge.[19–21] The formation of oxygen vacancies is particularly common in

[a] *Department of Chemistry and Biochemistry, University of Arkansas, Fayetteville, USA. E-mail: chenj@uark.edu*
[b] *Institute of Nanoscience and Engineering, University of Arkansas, Fayetteville, USA*
[c] *Department of Chemistry and Biochemistry, University of Nevada, Las Vegas (UNLV), USA*
[d] *Institute for Photon Science and Synchrotron Radiation (IPS) and Institute for Chemical Technology and Polymer Chemistry (ITCP), Karlsruhe Institute of Technology (KIT), Karlsruhe, Germany*
[e] *Department of Chemical Engineering, Pennsylvania State University, USA. E-mail: greenlee@psu.edu*

† Electronic supplementary information (ESI) available. See DOI: https://doi.org/10.1039/d2ma00604a

compounds that theoretically contain a large amount of Fe(IV). For example, a full substitution of La(III) with Sr(II) to yield $SrFeO_{3-\delta}$ is expected to contain only Fe(IV) if it is fully oxygenated (*i.e.*, $SrFeO_3$), but in practice, its oxygen deficiency can vary from $\delta = 0$ to $\delta = 0.5$, depending on the synthesis conditions.[22–24] The oxygen stoichiometry of the $La_{1-x}Sr_xFeO_{3-\delta}$ perovskites strongly depends on the synthesis conditions, especially the final annealing temperature and oxygen partial pressure. With the substitution of La(III) with Sr(II), the formation energy of oxygen vacancies in $La_{1-x}Sr_xFeO_{3-\delta}$ decreases significantly and, as a result, the compound tends to be oxygen deficient.[25] For example, the $La_{1-x}Sr_xFeO_{3-\delta}$ compounds with $x \leq 2/3$ are essentially free of oxygen vacancies (*i.e.*, $\delta = 0$) when they are annealed in air and then cooled down slowly. However, for the compounds with $x > 2/3$, it is impossible to remove the oxygen vacancies by annealing in air, and the oxygen vacancy concentration increases with the Sr doping level.[20,26]

Being able to tune or reduce the number of oxygen vacancies in the $La_{1-x}Sr_xFeO_{3-\delta}$ perovskites has drawn considerable attention, because they exhibit a mixed ionic and electronic conductivity,[1,27,28] suited for electrocatalysis[29,30] and oxygen storage,[31] and Fe(IV) is particularly critical for understanding the oxygen evolution reaction (OER) mechanisms in Fe-doped NiOOH electrocatalysts.[29] The oxygen deficiency of $La_{1-x}Sr_xFeO_{3-\delta}$ could be finely tuned in the range of $\delta = 0$ to $\delta = 0.5$ by annealing the compounds under a controlled environment. For example, either rapid quenching at high temperatures or annealing under a low oxygen partial pressure, an inert atmosphere (*e.g.*, Ar), or a reducing atmosphere (*e.g.*, 1% H_2 in Ar), could introduce more oxygen vacancies into the crystalline structure.[20,21,32] However, it is hard to eliminate oxygen vacancies at $x \geq 2/3$ even when annealing under pure oxygen is performed.[19–21,32] It is even more difficult to yield the fully oxygenated $SrFeO_3$ without extreme conditions, that is, under pure oxygen at extremely high pressure ($\geq$20 MPa).[22,33,34]

In this work, we have developed an ozone treatment method which can greatly suppress the formation of oxygen vacancies in $La_{1-x}Sr_xFeO_{3-\delta}$ with $x \geq 2/3$, including $SrFeO_{3-\delta}$. Ozone is a strong oxidant that has been used to reduce oxygen vacancies; however, these ozone methods were limited to post-treatment, or in some cases coupled with ultraviolet (UV) radiation,[35,36] for the removal of the surface oxygen vacancies of metal oxides.[37] To our knowledge, ozone has not yet been demonstrated to reduce the oxygen vacancies of the bulk, especially for those cases in which full oxygenation of the bulk is difficult to achieve without a high-pressure oxygen treatment. This study demonstrates a new approach beyond the simple post-treatment in which ozone is applied *in situ* during the cooling process of the synthesis. A series of powder samples of $La_{1-x}Sr_xFeO_{3-\delta}$ (x = 0.0, 0.2, 0.4, 0.6, 0.8, and 1.0) were first synthesized using a polymerized complex method. The crystal structures of these samples were characterized using X-ray powder diffraction (XRD) and a Rietveld refinement. The content of Fe(IV) and oxygen vacancies in the samples were determined by redox titration. Ozone treatments were then applied to treat those samples with oxygen deficiency (*i.e.*, $La_{0.2}Sr_{0.8}FeO_{3-\delta}$ and $SrFeO_{3-\delta}$) while varying temperature, duration, and cooling rate. It was found that a slow cooling rate is the key to achieving high oxygen stoichiometry. As a result, highly oxygenated compounds, including $La_{0.2}Sr_{0.8}FeO_{2.994}$ and $SrFeO_{2.979}$, were successfully synthesized *via* ozone treatment at 225 °C for 6 h with subsequent slow cooling to 25 °C at 0.05 °C min^{-1}. Our findings demonstrate that ozone treatment under atmospheric pressure can replace the high-pressure oxygen annealing in previous studies for the synthesis of highly oxygenated $La_{1-x}Sr_xFeO_{3-\delta}$ perovskites with high Sr/La ratios ($x \geq 2/3$).

2. Experimental method

Chemicals and materials

Lanthanum(III) nitrate hexahydrate ($La(NO_3)_3{\cdot}6H_2O$, 99.9%), strontium nitrate ($Sr(NO_3)_2$, ACS grade, 99.0% min), iron(III) nitrate nonahydrate ($Fe(NO_3)_3{\cdot}9H_2O$, ACS, 98.0 + %), ethylenediaminetetraacetic acid (EDTA, 99%), citric acid (anhydrous, ACS grade, 99.5 + %), ammonium hydroxide (NH_4OH, 28% NH_3), hydrochloric acid (HCl, 99.999% (metals basis), 36.5% min), 1,10-phenanthroline iron(II) sulfate (0.025M aq. soln.), and cerium(IV) sulfate ($Ce(SO_4)_2$, 0.1 N standardized solution) were purchased from Alfa Aesar. Ammonium iron(II) sulfate hexahydrate ($(NH_4)_2Fe(SO_4)_2{\cdot}6H_2O$, Mohr's salt, 99.997% trace metals basis), phosphoric acid (H_3PO_4, 85 wt% in H_2O, 99.99% trace metals basis), and iron(III) oxide (Fe_2O_3, $\geq$99.995% trace metals basis) were purchased from Sigma-Aldrich. Ultrahigh-purity-grade oxygen (O_2, OX UHP300) and ultrahigh-purity-grade argon (Ar, AR UHP300) were purchased from Airgas. All chemicals and materials were used as received, unless specified otherwise. Ultrapure 18 MΩ cm water was used in all experiments.

Synthesis of $La_{1-x}Sr_xFeO_{3-\delta}$ (x = 0.0, 0.2, 0.4, 0.6, 0.8, 1.0)

The $La_{1-x}Sr_xFeO_{3-\delta}$ powder samples were synthesized using a polymerized complex method.[38] For the synthesis of $LaFeO_3$, 40 mmol of EDTA was mixed with 40 ml of 1 M NH_4OH solution in a 500 mL beaker, and then 20 mmol of $La(NO_3)_3{\cdot}6H_2O$, 20 mmol of $Fe(NO_3)_3{\cdot}9H_2O$, and 60 mmol of citric acid were added to the solution under magnetic stirring. The solution pH was then adjusted to 8.0 by adding 1 M NH_4OH solution. The resulting solution was heated on a hot plate with a surface temperature of 135 °C and stirred at 340 rpm for 24 h to form a viscous gel. The obtained gel was then heated in a muffle furnace (Thermolyne 6000, Thermo Scientific) at 200 °C for 6 h to form a powder. [Caution: the reaction mixture expands vigorously and generates a large amount of smoke during the heating; therefore, this process must be carried out in a fume hood with sufficient ventilation. To prevent significant sample loss due to the expansion of the reaction mixture, the beaker containing the gelled sample was placed in a 1-gallon wide-mouth glass jar (Fig. S1, ESI†) that was then placed inside the furnace chamber.] After the heat treatment was completed, the sample powder was collected, ground carefully using a mortar and pestle, and then calcined in the muffle furnace at 900 °C for 5 h in air. The as-obtained power was ground again and then calcined in a high-temperature furnace (KSL-1700X, MTI Corporation) at

1300 °C for 4 h in air, with the heating and cooling rates set to 5 °C min^{-1}. The final product was ground and stored under ambient conditions for future use.

For the samples containing Sr, *i.e.*, $La_{1-x}Sr_xFeO_{3-\delta}$ with x = 0.2, 0.4, 0.6, 0.8, and 1.0, the same method was used, but the La precursor was replaced by the Sr precursor in the synthesis, according to the corresponding molar ratio. For the synthesis of $La_{0.2}Sr_{0.8}FeO_{3-\delta}$ and $SrFeO_{3-\delta}$, impurities were found in the final product when a large amount of the sample powder was calcined at 1300 °C using a single alumina crucible (cylindrical with covering lid, diameter: 40 mm, height: 40 mm, MTI corporation). To prevent this issue, high-purity samples were synthesized using the following protocols: for $La_{0.2}Sr_{0.8}FeO_{3-\delta}$, the sample powder was equally separated into 8 alumina crucibles, with 4 of them calcined at 1300 °C at a time. For $SrFeO_{3-\delta}$, the sample powder was equally separated into 16 alumina crucibles, with 2 of them calcined at 1300 °C at a time.

Ozone treatment of $SrFeO_{3-\delta}$ and $La_{0.2}Sr_{0.8}FeO_{3-\delta}$

The ozone treatment was carried out under atmospheric pressure in a horizontal 1 inch diameter quartz tube furnace (Lindberg/Blue M, Model TF55035A-1), connected to a commercial ozone generator (Enaly, Model 5000BF-1), as shown in Fig. S2 (ESI†). The $SrFeO_{3-\delta}$ or $La_{0.2}Sr_{0.8}FeO_{3-\delta}$ powder was evenly spread in a quartz boat to maximize the contact between the sample particles and the gas flow. The quartz boat was then placed inside the quartz tube and positioned at the center of the tube furnace. In a typical process, the sample was flushed with oxygen for 30 min to ensure that the sample was under pure oxygen environment. Then, the furnace temperature was increased from room temperature to 650 °C at the rate of 5 °C min^{-1} and kept at that temperature for 6 h. Immediately after, the furnace temperature was decreased to the ozone treatment temperature (200–400 °C) at the rate of 5 °C min^{-1} and then kept at that temperature for 2–6 h. The ozone generator was turned on when the furnace temperature reached the ozone treatment temperature. After ozone treatment, the sample was cooled to room temperature under the ozone environment. The ozone generator used in this study can provide ozone at 5% concentration when the oxygen flow rate is ~750 mL min^{-1}. Given that the ozone treatment was operated at a lower oxygen flow rate, the ozone concentration in all experiments is 5% minimum (min. 5%).

X-Ray diffraction and Rietveld refinement

The crystalline structures of the samples were determined by XRD using Cu K_α radiation (Philips PW1830). The diffraction patterns were collected over a 2θ range of 10–90° using a step size of 0.025° at 3 s per step, corresponding to ~2.7 h of collection time for each measurement to produce an acceptable signal-to-noise ratio. The obtained data were analyzed by the Rietveld method[39] using the FullProf Suite program.[40] Initial models of the crystal structures, in the format of Crystallographic Information Files (.cif), were obtained from the Crystallography Open Database (COD).[41–47] The line shape of the diffraction peaks was modelled using a pseudo-Voigt function, and the background was refined to a linear interpolation between a set of background points with refinable heights. Note that the site occupancy factors for the oxygen ions were not refined since it is difficult to obtain accurate values from the refinement of powder XRD data. Instead, the most abundant phase in each sample was determined by fitting the experimental data with multiple model crystal structures with known site occupancy factors that are available from the COD. The model crystal structure that could best fit the experimental data and result in a reasonable Fe–O bond distance is considered the dominant phase of the sample for refinement.

Redox titration

The concentrations of Fe(IV) (y) and oxygen vacancies (δ) in the $La_{1-x}Sr_xFeO_{3-\delta}$ compounds were quantified by redox titration.[19,48] All glassware and magnetic stir bars were cleaned with mild detergent, soaked overnight in a 10% nitric acid bath, washed thoroughly with deionized water, and rinsed thoroughly with ultrapure 18 MΩ cm water. The titration procedure starts by adding 50 ml of 6 M HCl to the flask, which is then purged with ultrahigh-purity-grade Ar for 5 min under stirring at 200 rpm to remove atmospheric oxygen; the titration set-up is shown in Fig. S3 (ESI†). The entire titration process was performed under continuous Ar flow. Then, ~0.1 g of Mohr's salt, containing Fe(II), and ~0.05 g of the sample powder were added to the solution, followed by rinsing the walls of the flask with 5 ml of 6 M HCl to ensure that all of the added Mohr's salt and the sample powder was rinsed into the solution. After purging with Ar for another 5 min while stirring, the reaction mixture was heated to fully dissolve the sample powder, whose Fe(IV) component is reduced by Fe(II) of the Mohr's salt to yield Fe(III). The temperature and heating time required for the complete dissolution of each sample are listed in Table S1 (ESI†). After complete dissolution, the reaction mixture was cooled down in a water-ice bath for 10 min. Then, 5 mL of 85 wt% H_3PO_4 was added to the titrate to form a colorless complex with Fe(III), followed by adding one drop of 0.025 M 1,10-phenanthroline iron(II) sulfate as an indicator. Finally, the excess of Fe(II) from the Mohr's salt in the solution was titrated with a 0.015 M $Ce(SO_4)_2$ solution. The end point of the titration was indicated by a sudden color change of the solution from red-orange to colorless or light blue. Each sample was titrated three times to report the mean values and standard errors.

The Fe(IV) concentration (y) and the oxygen vacancy (δ) in $La_{1-x}Sr_xFe(III)_{1-y}Fe(IV)_yO_{3-\delta}$ can be calculated using the eqn (1) and (2), based on the charge balance of the chemical formula and the number of moles of Fe(IV) (n, in mol) in a sample with measured mass (m, in g) determined by the titration.

Charge balance:

$$3(1 - x) + 2x + 3(1 - y) + 4y = 2(3 - \delta) \quad (1)$$

Fe(IV) determined by titration:

$$ym/[M_{La}(1 - x) + M_{Sr}x + M_{Fe} + M_o(3 - \delta) = n] \quad (2)$$

where M_{La}, M_{Sr}, M_{Fe}, and M_o is molar mass of La (138.905 g mol^{-1}), Sr (87.62 g mol^{-1}), Fe (55.845 g mol^{-1}), and O (15.999 g mol^{-1}).

Using the eqn (2) minus m times eqn (1), the oxygen vacancy is obtained by eqn (3).

$$\delta = (242.747n - 51.285nx - mx)/(15.999n - 2m) \quad (3)$$

With δ known, the Fe(IV) concentration can be calculated using eqn (4).

$$y = x - 2\delta \quad (4)$$

The stoichiometries of La $(1 - x)$ and Sr $(x, 0 \leq x \leq 1)$ are obtained from the molar ratio of the precursors and confirmed by inductively coupled plasma mass spectrometry (ICP-MS) measurement.

3. Results and discussion

3.1. Elemental composition and crystalline structure of $La_{1-x}Sr_xFeO_{3-\delta}$ calcined in air

A series of $La_{1-x}Sr_xFeO_{3-\delta}$ (x = 0.0, 0.2, 0.4, 0.6, 0.8, 1.0) samples were synthesized using a polymerized complex method by first forming the gel from the basic solution of La, Sr, and Fe precursors in the presence of EDTA and citric acid, and then calcining the gel at sequential elevated temperatures to yield the perovskite oxide powders. Fig. 1 illustrates the reaction scheme, along with the crystal structure and the stoichiometry of each resulting compound obtained from XRD Rietveld refinement and redox titration. It was found that the cooling rate of the last calcination step is the key to control the oxygen deficiency in these compounds. The slow cooling rate allows the perovskite oxides to take up oxygen from the atmosphere, leading to a (partial) filling of oxygen vacancies.[49] In the synthesis, the cooling rate was kept at 5 °C min^{-1} for the last calcination step. The elemental composition of the resulting $La_{1-x}Sr_xFeO_{3-\delta}$ compounds was analyzed using ICP-MS. The measured molar ratios of La/Fe and Sr/Fe were very close to the theoretical values of $1 - x$ and x, respectively, with the differences between the measured and theoretical ratios less than 0.015 (Fig. S4, ESI†). The results suggest that the reaction gives nearly 100 percent yield for the conversion of La, Sr, and Fe precursors to the corresponding perovskite oxide compounds.

These $La_{1-x}Sr_xFeO_{3-\delta}$ compounds were characterized by XRD to determine their corresponding crystal structures. Fig. 2 displays the XRD patterns of the $La_{1-x}Sr_xFeO_{3-\delta}$ compounds with x = 0, 0.2, 0.4, 0.6, 0.8, and 1.0. The XRD peak positions and their relative intensities are, in general, consistent with previously reported data for these compounds, prepared using a solid-state reaction or the Pechini method.[49–51] To further confirm the crystal structure and estimate structural parameters such as lattice constants and atomic distances, we performed a Rietveld refinement on each of these XRD patterns based on known structural information in the literature. For example, it is known that fully oxygenated $La_{1-x}Sr_xFeO_3$ (*i.e.*, $\delta = 0$) undergoes phase changes as the Sr composition increases, from an orthorhombic phase (*Pbnm*) for $0 \leq x \leq 0.2$, to a rhombohedral phase ($R\bar{3}c$) for $0.4 \leq x \leq 0.7$, and a cubic phase ($Pm\bar{3}m$) for $0.8 \leq x \leq 1.0$.[19,32,34,50] We also took into consideration the oxygen vacancy effects on the crystal structure in choosing the initial model crystal structures for refinement. This is particularly important for the compounds with Sr composition $x > 0.6$, where a significant amount of oxygen vacancies were found,[20] and where the ordering of oxygen vacancies had a profound effect on the crystal structure.[22,32,50] For example, the fully substituted end-member, $SrFeO_{3-\delta}$, was found to have the following four different crystal structures, depending on the oxygen stoichiometry: $SrFeO_3$ (cubic, space group $Pm\bar{3}m$), $SrFeO_{2.875}$ (tetragonal, space group $I4/mmm$), $SrFeO_{2.75}$ (orthorhombic, space group *Cmmm*), and $SrFeO_{2.5}$ (orthorhombic, *Ibm*2).[22] Based on this knowledge, the experimental XRD patterns of $La_{1-x}Sr_xFeO_{3-\delta}$ compounds with $0 \leq x \leq 0.6$ fit well with the calculated patterns for the corresponding structures of the fully-oxygenated

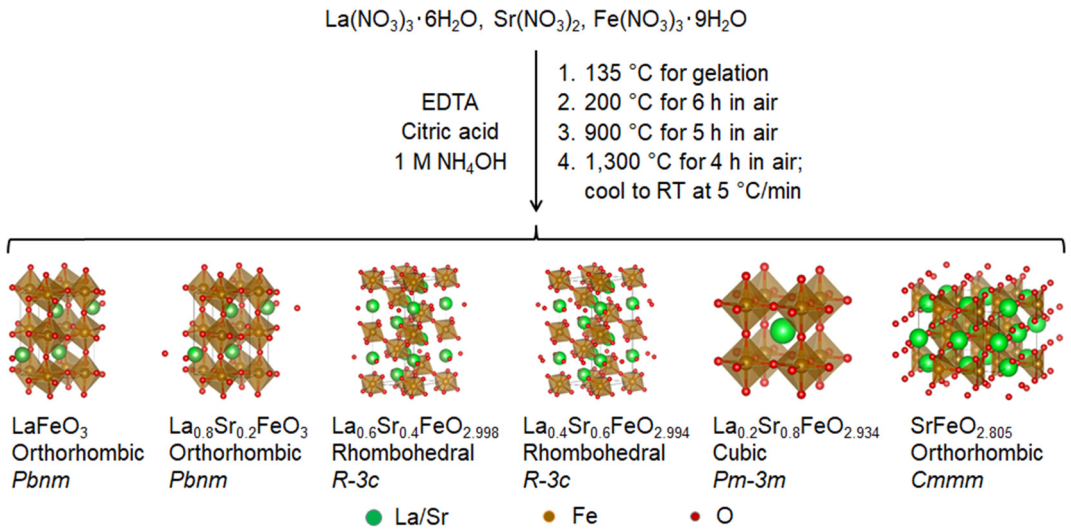

Fig. 1 Reaction scheme of $La_{1-x}Sr_xFeO_{3-\delta}$ compounds *via* a polymerized complex method and calcined in air. The crystal structures were obtained from Rietveld refinements of the XRD patterns and the oxygen stoichiometry was determined by redox titration.

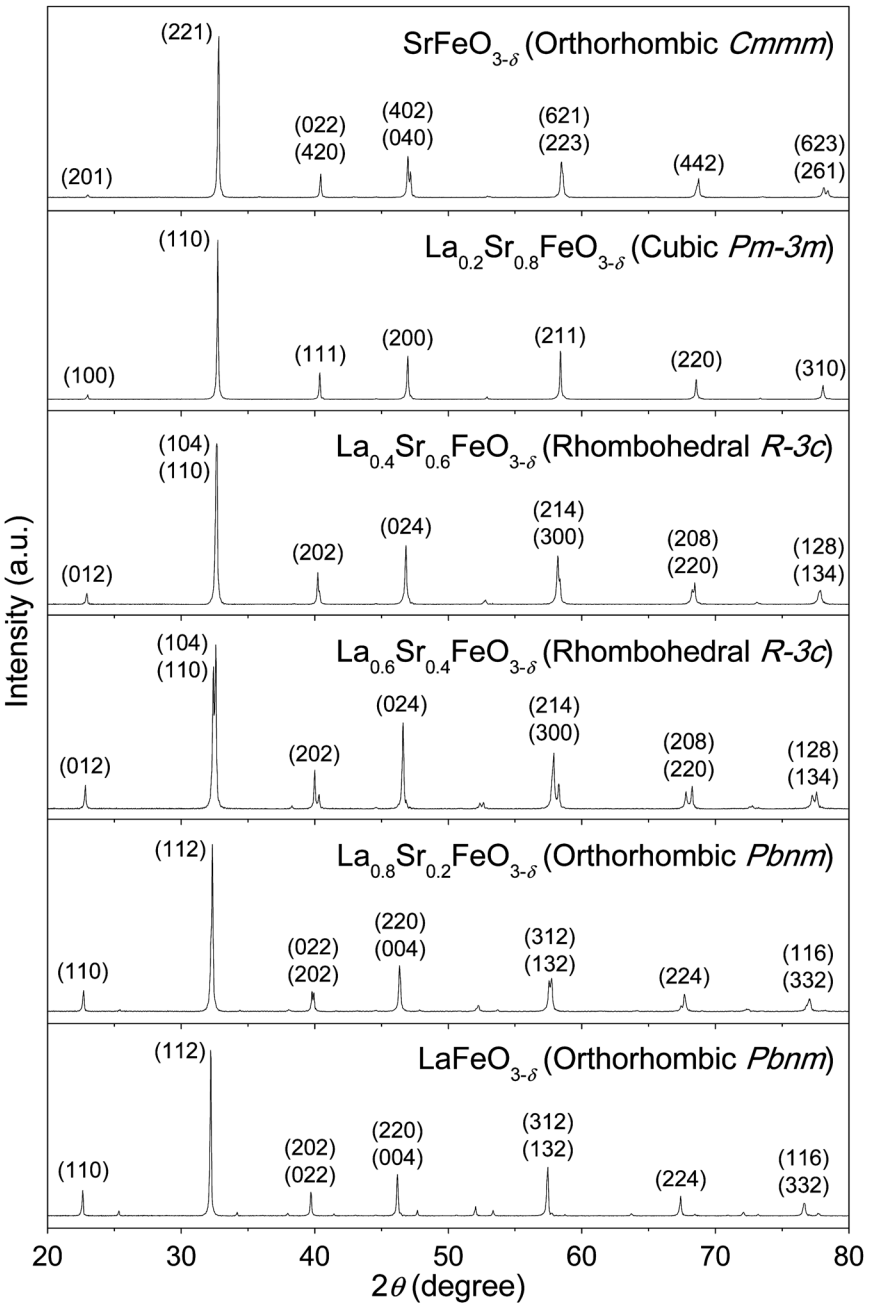

Fig. 2 Powder XRD patterns of $La_{1-x}Sr_xFeO_{3-\delta}$ compounds, synthesized using a polymerized complex method and calcined in air, as described in Fig. 1. The patterns were indexed according to the calculated patterns generated using the VESTA software and the crystallographic information files obtained from the Rietveld refinement.

$La_{1-x}Sr_xFeO_3$ ($\delta = 0$). For $La_{0.2}Sr_{0.8}FeO_{3-\delta}$, a reasonable agreement between the observed diffraction data and calculated profile was achieved using a $Pm\bar{3}m$ cubic structural model with oxygen stoichiometry of 2.96 (*i.e.*, $La_{0.2}Sr_{0.8}FeO_{2.96}$). This model was chosen based on literature suggestions that $La_{0.2}Sr_{0.8}FeO_{3-\delta}$ prepared using a solid-state reaction method with annealing at 1230 °C for 48 h and then furnace cooling to room temperature had an oxygen stoichiometry of 2.96.[20] For $SrFeO_{3-\delta}$, the experimental XRD patterns were refined by the four above-mentioned crystal structures (Fig. S5 and S6, ESI†). Based on the results, there could be two phases co-existing in our $SrFeO_{3-\delta}$ compound, with a major phase of $SrFeO_{2.75}$ (orthorhombic, space group *Cmmm*) and a minor phase of $SrFeO_{2.875}$ (tetragonal, space group *I*4/*mmm*).

The Rietveld refinement results are plotted in Fig. S7 (ESI†) by overlaying the experimental and calculated patterns for each compound. The structure of each compound refined by the Rietveld method is presented in Fig. 1. The data obtained from the Rietveld method are listed in Table 1. A gradual decrease in the Fe–O bond length with increasing Sr was found, from

x = 0.0 to x = 0.8. The lengths of Fe–O bonds in iron oxides are typically 1.91–1.95 Å, 1.990–2.006 Å, and about 2.14 Å for Fe(IV), Fe(III), and Fe(II), respectively.[49] These results indicate that an increased percentage of Fe in $La_{1-x}Sr_xFeO_{3-\delta}$ is oxidized from Fe(III) to Fe(IV) with increasing Sr content up to x = 0.8. For the fully-substituted end-member $SrFeO_{3-\delta}$, however, the presence of a large quantity of oxygen vacancies results in the reduction of Fe(IV) to Fe(III). The exact content of Fe(IV) in the $La_{1-x}Sr_xFeO_{3-\delta}$ compounds needs to be determined in order to verify the findings from the XRD analysis, as will be done in the following.

The content of Fe(IV) and the associated oxygen stoichiometry in the $La_{1-x}Sr_xFeO_{3-\delta}$ compounds were determined using redox titration. As illustrated in Fig. 3a, the titration involves a two-step process in which the Fe(IV) in the $La_{1-x}Sr_xFeO_{3-\delta}$ compound is first reacted with an excess amount of Fe(II), and then the remaining Fe(II) is titrated with a standard Ce(IV) solution. As a result, the number of moles of Fe(IV) in the $La_{1-x}Sr_xFeO_{3-\delta}$ compound equals the difference between the numbers of moles of the added Fe(II) and Ce(IV) consumed during the titration. The concentrations of Fe(IV) (y) and oxygen vacancies (δ) in each $La_{1-x}Sr_xFe(III)_{1-y}Fe(IV)_yO_{3-\delta}$ compound were calculated based on the amounts of the added Mohr's salt or Fe(II), the sample used, and the 0.015 M $Ce(SO_4)_2$ solution consumed during titration. The calculation is detailed in the Experimental Method section. The titration results are summarized in Table S2 (ESI†) and are highly reproducible, as indicated by the standard errors of less than 0.004.

The stoichiometry of Fe(IV) (y) and oxygen vacancy (δ) are plotted against the Sr content (x) in the $La_{1-x}Sr_xFe(III)_{1-y}Fe(IV)_yO_{3-\delta}$ compounds in Fig. 3b. A linear increase in y, the stoichiometry of Fe(IV), with increasing Sr composition (x) was observed until x = 0.6 ($y = 0.985x$ with R^2 = 0.9989). The slope of the linear fit is 0.985, suggesting that the substitution of La(III) by Sr(II) is nearly completely compensated by the conversion of Fe(III) to Fe(IV) in the $La_{1-x}Sr_xFeO_{3-\delta}$ perovskites (for $0 \leq x \leq 0.6$). In other words, the number of oxygen vacancies (δ) in these compounds is very small. However, when the Sr composition (x) was further increased from 0.6 to 1.0, the curve deviated from the low-x linear relationship, only reaching y = 0.667 at x = 0.8. At x = 1.0, we even find a slight decrease to y = 0.611. The results suggest that significant amounts of oxygen vacancies are introduced to the $La_{1-x}Sr_xFeO_{3-\delta}$ perovskites with $x > 0.6$. These observations are consistent with previous studies that show how the content of the oxygen vacancies increases with increased Sr composition and that it is impossible to achieve fully oxygenated compounds with Sr composition $x >$ 0.6 in air.[20,26] The results also corroborate the XRD analysis that the $SrFeO_{3-\delta}$ compound with oxygen stoichiometry of 2.805 would likely be a mixture of two different phases. This, in turn, agrees well with the previous finding that $SrFeO_{2.75}$ (orthorhombic, space group *Cmmm*) and $SrFeO_{2.875}$ (tetragonal, space group *I*4/*mmm*) can coexist in $SrFeO_{2.80}$.[23]

3.2. Ozone treatment of highly-oxygen deficient $La_{1-x}Sr_xFeO_{3-\delta}$ compounds

To increase the oxygen stoichiometry of the compounds with high content of Sr ($x > 0.6$), we applied an ozone treatment at ambient pressure as an alternative to oxygen treatment at high pressure. Ozone is a strong oxidizing agent, known to generate radicals and thus eliminate pathogens and other contaminants in water.[52] The radical mechanism makes it possible to fill the oxygen vacancies in highly oxygen-deficient compounds at mild conditions without the use of high pressure. Ozone treatment has been suggested to fully oxygenate the epitaxial $La_{1-x}Sr_xFeO_{3-\delta}$ films with thicknesses varying from 6.9 nm to 52.2 nm;[2,53–55] however, so far there has not been a direct evidence of whether full oxygen stoichiometry was achieved in these studies. In this study, we thus further developed the ozone treatment approach and monitored the changes of oxygen stoichiometry by redox titration to demonstrate that the ozone treatment can reverse the loss of oxygen in these high-Sr compounds (*i.e.*, $SrFeO_{3-\delta}$ and $La_{0.2}Sr_{0.8}FeO_{3-\delta}$).

The ozone treatment was carried out under min. 5% O_3/O_2 at ambient pressure. We investigated the effects of temperature, duration time, and cooling rate during ozone treatment on the Fe(IV) content and oxygen stoichiometry of the highest Sr containing compound, $SrFeO_{3-\delta}$, which is the most difficult one to be fully oxygenated. Fig. 4a–c, displays the correlation of the ozone treatment conditions and the changes of the Fe(IV) (y) and oxygen vacancy (δ) content of $SrFe(III)_{1-y}Fe(IV)_yO_{3-\delta}$, monitored by the redox titration. The detailed parameters of each experiment are listed in Table S3 (ESI†). For a fully oxygenated compound, it is

Table 1 Summary of the Rietveld refinement results for the as-synthesized $La_{1-x}Sr_xFeO_{3-\delta}$ compounds calcined in air

Sample (x)	0.0	0.2	0.4	0.6	0.8	1.0
Model	$LaFeO_3$	$La_{0.8}Sr_{0.2}FeO_3$	$La_{0.6}Sr_{0.4}FeO_3$	$La_{0.4}Sr_{0.6}FeO_3$	$La_{0.2}Sr_{0.8}FeO_{2.96}$	$SrFeO_{2.75}$
Space group	*Pbnm*	*Pbnm*	*R*$\bar{3}$*c*	*R*$\bar{3}$*c*	*Pm*$\bar{3}$*m*	*Cmmm*
a (Å)	5.5560	5.5521	5.5301	5.4989	3.8728	10.9522
b (Å)	5.5666	5.5249				7.7098
c (Å)	7.8558	7.8196	13.4294	13.4221		5.4707
V (Å^3)	242.96	239.87	355.67	351.48	58.09	461.94
χ^2	1.41	1.29	1.56	1.64	1.77	1.52
<Fe–O> (Å)	Fe–O1: 2.0235	Fe–O1: 1.9986	Fe–O: 1.9660	Fe–O: 1.9484	Fe–O: 1.9364	Fe1–O1: 1.9244
	Fe–O1: 1.9849	Fe–O1: 1.9641				Fe1–O3: 1.8806
	Fe–O2: 2.0174	Fe–O2: 1.9915				Fe2–O2: 1.9356
						Fe2–O3: 2.0028

Note: a, b, and c are the lattice constants, V is the cell volume, and χ^2 is the goodness-of-fit.

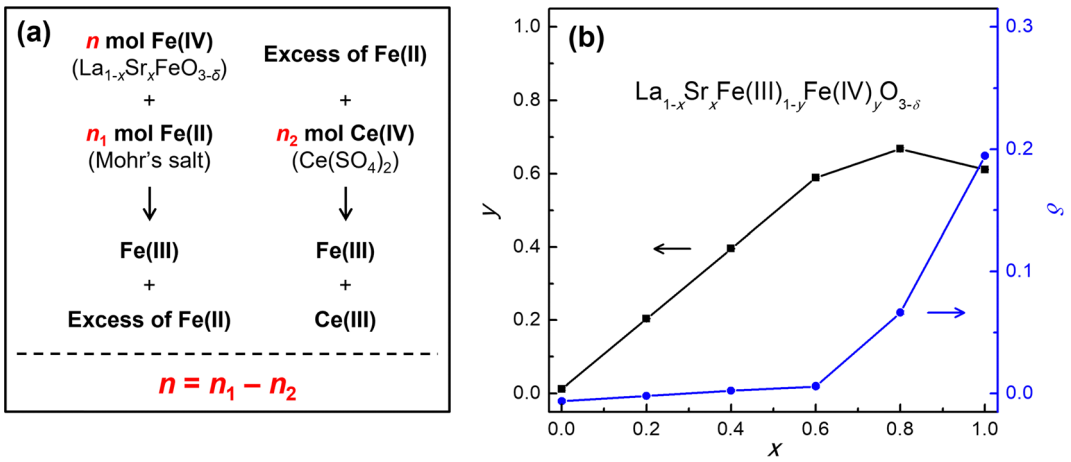

Fig. 3 (a) Schematic illustration of the working principle of the redox titration of Fe(IV). (b) Plot of the Fe(IV) (y, left ordinate) and oxygen vacancy (δ, right ordinate) content against Sr content (x) in the as-synthesized $La_{1-x}Sr_xFe^{(III)}_{1-y}Fe^{(IV)}_yO_{3-\delta}$ compounds calcined in air. The y and δ values were determined from the titration results detailed in the ESI.† The standard error is too small to be seen on the graph, but a full list of the data (including the standard errors) is listed in Table S2 (ESI†).

expected to have a stoichiometry of $SrFe^{(IV)}O_3$ with $y = 1$ and $\delta = 0$. We first studied the effect of temperature in the region of 200 to 400 °C (Fig. 4a; E2 to E7 in Table S3, ESI†). It was hypothesized that an increased temperature could lower the activation barrier

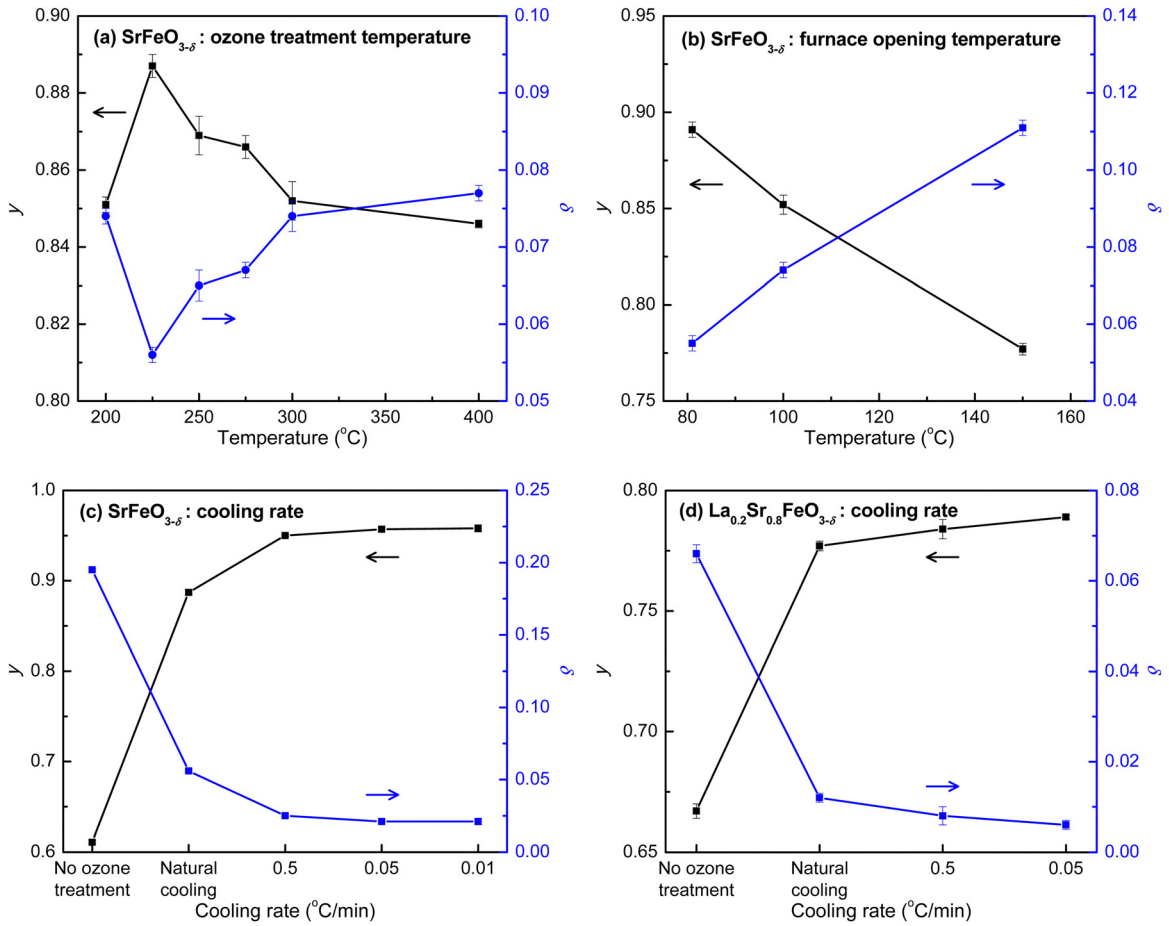

Fig. 4 Plots of Fe(IV) (y) and oxygen vacancies (δ) content of $SrFeO_{3-\delta}$ (a–c) and $La_{0.2}Sr_{0.8}FeO_{3-\delta}$ (d) *vs.* ozone treatment step at different conditions: (a) $SrFeO_{3-\delta}$ samples treated under ozone for 6 h at different temperatures, followed by cooling under ozone to 100 °C, followed by opening the furnace for fast cooling to room temperature; (b) $SrFeO_{3-\delta}$ samples treated under ozone for 6 h at 300 °C, followed by cooling under ozone to different furnace-opening temperatures; (c) $SrFeO_{3-\delta}$ and (d) $La_{0.2}Sr_{0.8}FeO_{3-\delta}$ samples treated under ozone for 6 h at 225 °C with different controlled cooling rates, compared to "natural cooling" and "no ozone treatment". The y and δ values were determined by the redox titration.

of the reaction based on the transition state theory (Arrhenius equation). However, the result indicated that with the increase of the ozone treatment temperature, the value of y first increased to reach the highest value of Fe(IV) at 0.887 obtained at 225 °C and then decreased (Fig. 4a). This implies that the temperature effect is not only to increase the rate of the forward reaction (k_f) – oxygenation reaction of the ozone treatment, but also to increase the rate of the reverse reaction (k_b) – deoxygenation reaction that causes the formation of oxygen vacancies.[23] The difference of the temperature effects on k_f and k_b appear to suggest an optimal temperature for the oxygenation ozone treatment at 225 °C. However, these experiments were done at a similar cooling rate by allowing the furnace to naturally cool to 100 °C, followed by opening the furnace cover for fast cooling to room temperature. In fact, we found that the content of Fe(IV) significantly increased when the cover of the furnace was opened at a lower temperature (Fig. 4b). Varying the temperature at which the furnace cover was opened, the value of y increased from 0.777 to 0.891 for opening at 150 and 80 °C, respectively. This result suggests that the cooling rate plays a significant role in controlling the k_f and k_b and shifts the oxygenation/deoxygenation reaction equilibrium during ozone treatment.

To further examine the effect of the cooling rate, the ozone treatment of $SrFeO_{3-\delta}$ was performed under a series of controlled cooling rates (E10 to E12 in Table S3, ESI†). The plot of y and δ against cooling rate in Fig. 4c indicates a significant increase in the content of Fe(IV) with decreased cooling rate. The values of y reached 0.950, 0.957, and 0.958 at cooling rates of 0.5, 0.05, and 0.01 °C min^{-1}, respectively. The value of y increased only slightly when the cooling rate decreased from 0.05 to 0.01 °C min^{-1}, indicating that the maximum value of y that could be obtained using this method is about 0.958. The corresponding highest oxygen stoichiometry can reach 2.979, which is within the range of those obtained *via* annealing under pure oxygen at high pressure (Table 2). The ozone treatment under controlled cooling rates was also carried out for $La_{0.2}Sr_{0.8}FeO_{3-\delta}$ (E13 to E15 in Table S3, ESI†). Similar to the trend of $SrFeO_{3-\delta}$, a significant increase in y was observed with decreasing cooling rate (Fig. 4d). The highest y value, reached at a cooling rate of 0.05 °C min^{-1}, was 0.789, which is only 0.13% different from the theoretical maximum value of 0.8, resulting in a stoichiometry of $La_{0.2}Sr_{0.8}FeO_{2.994}$ with nearly full oxygen occupation. The results demonstrate that the ozone treatment indeed offers a robust alternative to reverse the oxygen loss and fully oxygenate perovskites at atmospheric pressure.

The corresponding structures of the $SrFeO_{3-\delta}$ and $La_{0.2}Sr_{0.8}FeO_{3-\delta}$ compounds with different degrees of oxygenation were then characterized by XRD. The XRD patterns of the $SrFeO_{3-\delta}$ and $La_{0.2}Sr_{0.8}FeO_{3-\delta}$ compounds are shown at the top of Fig. S8 and S9 (ESI†), respectively. The oxygen vacancy concentration has a significant impact on the crystal structures of the $SrFeO_{3-\delta}$ and $La_{0.2}Sr_{0.8}FeO_{3-\delta}$ compounds, as seen by comparing the peak positions and shapes of the XRD patterns. Detail plots of the major XRD peaks are also shown in Fig. S8 and S9 (ESI†). The peak(s) of each XRD pattern at $2\theta = 47^\circ$ are displayed in Fig. 5 to further elaborate the changes obtained in the XRD patterns for these two sets of compounds, along with the crystal structure indices generated by the Rietveld refinement. This particular 2θ angle is chosen because one peak would arise for the cubic crystal structure, corresponding to the reflection plane (200) that is perpendicular to the c-axis of the cubic structure; however, two peaks would appear for the orthorhombic structure, with one indexed as (402) and the other indexed as (040).

For $SrFeO_{3-\delta}$, both the peak positions and shapes of the diffraction pattern at $2\theta \approx 47^\circ$ change significantly with increasing oxygen vacancy content (Fig. 5a). For the two near fully-oxygenated $SrFeO_{2.979}$ samples, a peak at 47.22° with a shoulder (of about half its intensity) at 47.34° can be assigned to the (200) reflection of the cubic structure. The peak splitting arises from the Cu Kα doublet of the X-ray source. The simulated pattern from Rietveld refinement of the experimental data yields a doublet at 47.18° and 47.30°, in agreement with our experimental observation. For the highly oxygen-deficient $SrFeO_{2.805}$, three peaks were identified (at 46.97°, 47.13°, and 47.29°), which can be indexed to the two doublet peaks for the (402) and (040) reflections of the orthorhombic structure. The Rietveld refinement of the orthorhombic structure, based on the experimental XRD data, yields simulated (402) reflections at 46.91° and 47.03°, and (040) reflections at 47.11° and 47.23°. The shoulder of the (402) peak at 47.03° overlaps with the major (040) peak at 47.11°, resulting in one broad peak observed in the experimental pattern. A structural transition from a cubic to an orthorhombic structure is observed in $SrFeO_{2.944}$, with the peak at 47.22° being broadened towards lower angles. The transition is more obvious in $SrFeO_{2.910}$, with the presence of a shoulder at 47.07°. As a result, the experimental diffraction patterns of $SrFeO_{2.910}$ and $SrFeO_{2.944}$ could not be fit using a single structural model in the Rietveld refinement.

For $La_{0.2}Sr_{0.8}FeO_{3-\delta}$, the peak shape remains very similar for all three compounds ($La_{0.2}Sr_{0.8}FeO_{2.994}$, $La_{0.2}Sr_{0.8}FeO_{2.988}$, and $La_{0.2}Sr_{0.8}FeO_{2.934}$), as shown in Fig. 5b. The observed doublet can be assigned to the (200) reflection of the cubic structure

Table 2 Comparison of the fully oxygenation of $SrFeO_{3-\delta}$ with δ close to zero using the ozone treatment developed in this work and the literature method by annealing under pure oxygen at high pressures

Compound	Temperature, time	Oxygen pressure	Cooling condition	Method for δ determination	Ref.
$SrFeO_{2.979}$	225 °C, 6 h	101.325 kPa	0.01 °C min^{-1} to RT	Redox titration	This work
$SrFeO_{2.998}$	400 °C, 24 h	30 MPa	1 °C h^{-1} to 200 °C	Thermogravimetric	22
$SrFeO_{2.961}$	450 °C, 24 h	20 MPa	N/A	Redox titration	19
$SrFeO_{2.98}$	900 °C, 12 h	20 MPa	5 °C min^{-1} to RT	Thermogravimetric	33
$SrFeO_{2.94}$	900 °C, —	35.5 MPa	Slowly cooled	Thermogravimetric	34

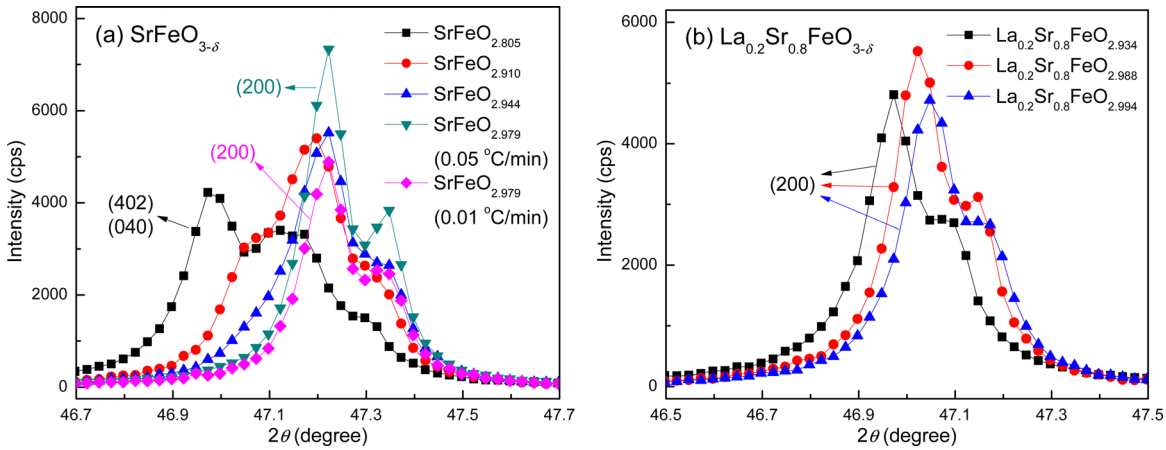

Fig. 5 XRD region centered at $2\theta = 47°$ for the ozone treated compounds: (a) $SrFeO_{3-\delta}$, and (b) $La_{0.2}Sr_{0.8}FeO_{3-\delta}$. The full XRD patterns are shown in Fig. S8 and S9 (ESI†).

based on the Rietveld refinement. As the number of oxygen vacancies increases, the peak shifts to lower angles, suggesting an increase of the lattice constant based on Bragg's Law. This finding is consistent with the Rietveld refinement results.

Table 3 summarizes the results of the Rietveld refinement of the experimental XRD patterns (cubic structures) for the near fully-oxygenated $SrFeO_{3-\delta}$ and $La_{0.2}Sr_{0.8}FeO_{3-\delta}$ compounds. A comparison of the simulated and experimental XRD patterns is shown in Fig. S10 (ESI†). A decrease in the Fe–O bond distance was observed when decreasing the number of oxygen vacancies in the $SrFeO_{3-\delta}$ and $La_{0.2}Sr_{0.8}FeO_{3-\delta}$ compounds, which indicates an increase in the oxidation state of Fe. These results are thus consistent with those obtained from the redox titration. For $SrFeO_{3-\delta}$, the Fe–O bond distances estimated from the refinement are 1.9262 Å for $SrFeO_{2.979}$ (0.05 °C min^{-1}) and 1.9248 Å for $SrFeO_{2.979}$ (0.01 °C min^{-1}). These values are consistent with the literature reported data of 1.91–1.95 Å for Fe(IV) in iron oxides,[49] indicating an oxidation state close to Fe(IV).

The ozone treatment at a slow cooling rate thus provides a robust approach to reverse the loss of oxygen in the $SrFeO_{3-\delta}$ and $La_{0.2}Sr_{0.8}FeO_{3-\delta}$ perovskite oxides under ambient pressure, as schematically shown in Fig. 6. The ozone generates radicals that can effectively react with the perovskite lattice and fill the oxygen vacancies in highly oxygen-deficient structures; however, simple ozone applied in post-treatment is not sufficient to fully oxygenate the bulk of these materials. The ozone treatment is required to be applied *in situ* during the cooling process, starting from an optimized temperature of 225 °C, at which the oxygenation is favorable. More importantly, a slower cooling rate facilitates the complete filling of the oxygen vacancies of the bulk. In this study, the cooling rate of 0.05 °C min^{-1}, starting from 225 °C, resulted in near-zero oxygen vacancies for the perovskites with high Fe(IV) content, quantified by the redox titration as $SrFeO_{2.979}$ and $La_{0.2}Sr_{0.8}FeO_{2.994}$. The crystal structures and stoichiometry of $SrFeO_{2.979}$ and $La_{0.2}Sr_{0.8}FeO_{2.994}$ compounds are stable in air at room temperature after storage for months, as confirmed by XRD and titration.

After ozone treatment, little changes were found in the morphology of the samples for both $SrFeO_{3-\delta}$ and $La_{0.2}Sr_{0.8}FeO_{3-\delta}$ compounds, as shown in Fig. S11 and S12 (ESI†). They consist of particulates with different sizes ranging from tens of nanometers to tens of micrometers. Based on the EDS analysis, the ratio of Sr to Fe in $SrFeO_{3-\delta}$ is approximately 1 : 1, and the ratio of La : Sr : Fe is close to the stoichiometry in formula of $La_{0.2}Sr_{0.8}FeO_{3-\delta}$. After storage under ambient conditions for 9 months, the crystal structures of the ozone-treated compounds (*i.e.*, $SrFeO_{2.979}$ and $La_{0.2}Sr_{0.8}FeO_{2.994}$) remain the same as the freshly-prepared samples (Fig. S13, ESI†). The titration results indicate that the Fe(IV) stoichiometry of ozone-treated $SrFeO_{3-\delta}$ at 0.01 °C min^{-1} only shows a slight decrease by 0.8%, and the Fe(IV) stoichiometry of ozone-treated $SrFeO_{3-\delta}$ and $La_{0.2}Sr_{0.8}FeO_{3-\delta}$ at 0.05 °C min^{-1} decreases by 1.8% and 1.5%, respectively (Table S3, ESI†). This

Table 3 Summary of the results from Rietveld refinement for the near fully-oxygenated $SrFeO_{3-\delta}$ and $La_{0.2}Sr_{0.8}FeO_{3-\delta}$ compounds

Samples	$SrFeO_{2.979}$ (0.05 °C min^{-1})	$SrFeO_{2.979}$ (0.01 °C min^{-1})	$La_{0.2}Sr_{0.8}FeO_{2.988}$	$La_{0.2}Sr_{0.8}FeO_{2.994}$
Model	$SrFeO_{2.96}$	$SrFeO_{2.96}$	$La_{0.2}Sr_{0.8}FeO_{2.96}$	$La_{0.2}Sr_{0.8}FeO_{2.96}$
Space group	$Pm\bar{3}m$	$Pm\bar{3}m$	$Pm\bar{3}m$	$Pm\bar{3}m$
a (Å)	3.8525	3.8496	3.8673	3.8665
b (Å)				
c (Å)				
V (Å^3)	57.18	57.05	57.84	57.80
χ^2	1.99	2.17	1.92	1.71
⟨Fe–O⟩ (Å)	Fe–O: 1.9262	Fe–O: 1.9248	Fe–O: 1.9337	Fe–O: 1.9333

Note: a, b, and c are the lattice constant. V is cell volume. χ^2 is goodness-of-fit.

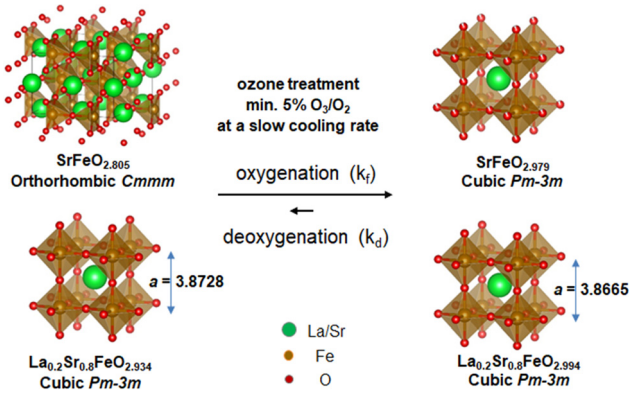

Fig. 6 Schematic illustration of the ozone treatment at a slow cooling rate, facilitating the oxygenation reaction to produce samples with near-ideal oxygen stoichiometry ($SrFeO_{2.979}$ and $La_{0.2}Sr_{0.8}FeO_{2.994}$).

method can couple to the commonly-used calcination method to offer a facile means to reduce oxygen vacancies without the need of high-pressure environments.

4. Conclusions

We have developed an ozone treatment method as a robust alternative to high pressure oxygen treatments to reverse the oxygen loss in the $La_{1-x}Sr_xFeO_{3-\delta}$ perovskites ($x > 0.6$). Using this method, we have successfully synthesized near fully-oxygenated $La_{0.2}Sr_{0.8}FeO_{2.994}$ and $SrFeO_{2.979}$ at ambient pressure. This method complements our synthesis of a series of $La_{1-x}Sr_xFeO_{3-\delta}$ (x = 0.0, 0.2, 0.4, 0.6, 0.8, and 1.0) compounds with near-ideal oxygen stoichiometry, in which annealing in air with slow cooling was sufficient to achieve full oxygen stoichiometry for $x \leq 0.6$. Since $La_{0.2}Sr_{0.8}FeO_{3-\delta}$ and $SrFeO_{3-\delta}$, however, showed significant amounts of oxygen vacancies when the compounds were calcined in air, we applied the above-mentioned heat-treatment in a mixture of ozone (min. 5%) and oxygen under atmospheric pressure at different conditions by varying temperature, duration, and cooling rate. It was found that the cooling rate is the key to obtaining high oxygen stoichiometry through an optimized balance of the rates of the oxygenation/deoxygenation reactions. In general, a significant increase in the oxygen content of $La_{0.2}Sr_{0.8}FeO_{3-\delta}$ and $SrFeO_{3-\delta}$ was observed with a decrease of the cooling rate. An ozone treatment at 225 °C for 6 h and subsequent cooling to 25 °C at 0.05 °C min^{-1} resulted in $La_{0.2}Sr_{0.8}FeO_{2.994}$ and $SrFeO_{2.979}$ under atmospheric pressure, achieving an oxygen concentration similar to the compounds obtained *via* annealing under pure oxygen at high pressure ($\geq$20 MPa). This ozone treatment, using controlled heating and cooling rates, offers an attractive alternative approach to high pressure methods for the synthesis of fully oxygenated perovskites and other complex oxides under atmospheric pressure.

Author contributions

Conceptualization, L. G., C. H., J. C.; methodology, G. Q., L. G., C. H., and J. C.; investigation, G. Q., D. T., and M. B.; data curation, G. Q., D. T., M. B., C. H., L. G., J. C.; writing – original draft preparation, G. Q.; writing – review and editing, G. Q., D. T., M. B., C. H., L. G., J. C.

Conflicts of interest

There are no conflicts to declare.

Acknowledgements

We gratefully acknowledge financial support for this work from the Department of Energy (Grant Number: DE-SC0021308).

References

1 T. Maeder and J. G. Bednorz, Influence of Oxygen Stoichiometry on Electrical Transport and Magnetic Properties of Doped Perovskite-Type Ferrate and Manganate Single Crystals, *J. Eur. Ceram. Soc.*, 1999, **19**, 1507–1510.
2 S. Y. Smolin, M. D. Scafetta, A. K. Choquette, M. Y. Sfeir, J. B. Baxter and S. J. May, Static and Dynamic Optical Properties of $La_{1-x}Sr_xFeO_{3-\delta}$: The Effects of a-Site and Oxygen Stoichiometry, *Chem. Mater.*, 2016, **28**, 97–105.
3 K. Y. Zhu, F. Shi, X. F. Zhu and W. S. Yang, The Roles of Oxygen Vacancies in Electrocatalytic Oxygen Evolution Reaction, *Nano Energy*, 2020, **73**, 104761.
4 L. Xu, Q. Q. Jiang, Z. H. Xiao, X. Y. Li, J. Huo, S. Y. Wang and L. M. Dai, Plasma-Engraved Co_3O_4 Nanosheets with Oxygen Vacancies and High Surface Area for the Oxygen Evolution Reaction, *Angew. Chem., Int. Ed.*, 2016, **55**, 5277–5281.
5 J. Kim, X. Yin, K. C. Tsao, S. H. Fang and H. Yang, $Ca_2Mn_2O_5$ as Oxygen-Deficient Perovskite Electrocatalyst for Oxygen Evolution Reaction, *J. Am. Chem. Soc.*, 2014, **136**, 14646–14649.
6 J. R. Petrie, H. Jeen, S. C. Barron, T. L. Meyer and H. N. Lee, Enhancing Perovskite Electrocatalysis through Strain Tuning of the Oxygen Deficiency, *J. Am. Chem. Soc.*, 2016, **138**, 7252–7255.
7 F. Y. Cheng, T. R. Zhang, Y. Zhang, J. Du, X. P. Han and J. Chen, Enhancing Electrocatalytic Oxygen Reduction on MnO_2 with Vacancies, *Angew. Chem., Int. Ed.*, 2013, **52**, 2474–2477.
8 L. L. Li, Z. J. Zhao, C. L. Hu, P. P. Yang, X. T. Yuan, Y. N. Wang, L. Zhang, L. Moskaleva and J. L. Gong, Tuning Oxygen Vacancies of Oxides to Promote Electrocatalytic Reduction of Carbon Dioxide, *ACS Energy Lett.*, 2020, **5**, 552–558.
9 Z. G. Geng, X. D. Kong, W. W. Chen, H. Y. Su, Y. Liu, F. Cai, G. X. Wang and J. Zeng, Oxygen Vacancies in Zno Nanosheets Enhance CO_2 Electrochemical Reduction to CO, *Angew. Chem., Int. Ed.*, 2018, **57**, 6054–6059.
10 K. B. Chu, F. Z. Liu, J. W. Zhu, H. Fu, H. Y. Zhu, Y. L. Zhu, Y. Zhang, F. L. Lai and T. X. Liu, A General Strategy to Boost Electrocatalytic Nitrogen Reduction on Perovskite Oxides via the Oxygen Vacancies Derived from a-Site Deficiency, *Adv. Energy Mater.*, 2021, **11**, 2003799.

11 H. T. Xie, H. B. Wang, Q. Geng, Z. Xing, W. Wang, J. Y. Chen, L. Ji, L. Chang, Z. M. Wang and J. Mao, Oxygen Vacancies of Cr-Doped CeO_2 Nanorods That Efficiently Enhance the Performance of Electrocatalytic N_2 Fixation to NH_3 under Ambient Conditions, *Inorg. Chem.*, 2019, **58**, 5423–5427.

12 Y. Hou, J. Wang, C. X. Hou, Y. Q. Fan, Y. J. Zhai, H. Y. Li, F. Dang and S. L. Chou, Oxygen Vacancies Promoting the Electrocatalytic Performance of CeO_2 Nanorods as Cathode Materials for Li-O_2 Batteries, *J. Mater. Chem. A*, 2019, **7**, 6552–6561.

13 Y. H. Zou, W. Zhang, N. Chen, S. Chen, W. J. Xu, R. S. Cai, C. L. Brown, D. J. Yang and X. D. Yao, Generating Oxygen Vacancies in MnO Hexagonal Sheets for Ultralong Life Lithium Storage with High Capacity, *ACS Nano*, 2019, **13**, 2062–2071.

14 B. Qiu, *et al.*, Gas-Solid Interfacial Modification of Oxygen Activity in Layered Oxide Cathodes for Lithium-Ion Batteries, *Nat. Commun.*, 2016, **7**, 12108.

15 S. Zhang, Z. Jia, B. Cheng, Z. Zhao, F. Lu and G. Wu, Recent Progress of Perovskite Oxides and Their Hybrids for Electromagnetic Wave Absorption: A Mini-Review, *Adv. Compos. Hybrid Mater.*, 2022, 1–22.

16 Y. Liu, Z. Jia, Q. Zhan, Y. Dong, Q. Xu and G. Wu, Magnetic Manganese-Based Composites with Multiple Loss Mechanisms Towards Broadband Absorption, *Nano Res.*, 2022, **15**, 5590–5600.

17 Z. Jia, M. Kong, B. Yu, Y. Ma, J. Pan and G. Wu, Tunable Co/ZnO/C@MWCNTs Based on Carbon Nanotube-Coated Mof with Excellent Microwave Absorption Properties, *J. Mater. Sci. Technol.*, 2022, **127**, 153–163.

18 Y. Liu, X. Zhou, Z. Jia, H. Wu and G. Wu, Oxygen Vacancy-Induced Dielectric Polarization Prevails in the Electromagnetic Wave-Absorbing Mechanism for Mn-Based MOFs-Derived Composites, *Adv. Funct. Mater.*, 2022, **32**, 2204499.

19 J. Blasco, B. Aznar, J. Garcia, G. Subias, J. Herrero-Martin and J. Stankiewicz, Charge Disproportionation in $La_{1-x}Sr_xFeO_3$ Probed by Diffraction and Spectroscopic Experiments, *Phys. Rev. B: Condens. Matter Mater. Phys.*, 2008, **77**, 054107.

20 J. Cheng, A. Navrotsky, X. D. Zhou and H. U. Anderson, Thermochemistry of $La_{1-x}Sr_xFeO_{3-\delta}$ Solid Solutions ($0.0 \leq x \leq 1.0$, $0.0 \leq \delta \leq 0.5$), *Chem. Mater.*, 2005, **17**, 2197–2207.

21 J. B. Yang, W. B. Yelon, W. J. James, Z. Chu, M. Kornecki, Y. X. Xie, X. D. Zhou, H. U. Anderson, A. G. Joshi and S. K. Malik, Crystal Structure, Magnetic Properties, and Mössbauer Studies of $La_{0.6}Sr_{0.4}FeO_{3-\delta}$ Prepared by Quenching in Different Atmospheres, *Phys. Rev. B: Condens. Matter Mater. Phys.*, 2002, **66**, 184415.

22 J. P. Hodges, S. Short, J. D. Jorgensen, X. Xiong, B. Dabrowski, S. M. Mini and C. W. Kimball, Evolution of Oxygen-Vacancy Ordered Crystal Structures in the Perovskite Series $Sr_nFe_nO_{3n-1}$ ($n = 2, 4, 8$, and ∞), and the Relationship to Electronic and Magnetic Properties, *J. Solid State Chem.*, 2000, **151**, 190–209.

23 Y. Takeda, K. Kanno, T. Takada, O. Yamamoto, M. Takano, N. Nakayama and Y. Bando, Phase Relation in the Oxygen Nonstoichiometric System, $SrFeO_x$ ($2.5 \leq x \leq 3.0$), *J. Solid State Chem.*, 1986, **63**, 237–249.

24 J. B. MacChesney, R. C. Sherwood and J. F. Potter, Electric and Magnetic Properties of the Strontium Ferrates, *J. Chem. Phys.*, 1965, **43**, 1907–1913.

25 A. M. Ritzmann, A. B. Munoz-Garcia, M. Pavone, J. A. Keith and E. A. Carter, Ab Initio DFT+U Analysis of Oxygen Vacancy Formation and Migration in $La_{1-x}Sr_xFeO_{3-\delta}$ ($x = 0$, 0.25, 0.50), *Chem. Mater.*, 2013, **25**, 3011–3019.

26 J. Mizusaki, M. Yoshihiro, S. Yamauchi and K. Fueki, Nonstoichiometry and Defect Structure of the Perovskite-Type Oxides $La_{1-x}Sr_xFeO_{3-\delta}$, *J. Solid State Chem.*, 1985, **58**, 257–266.

27 M. Sogaard, P. V. Hendriksen and M. Mogensen, Oxygen Nonstoichiometry and Transport Properties of Strontium Substituted Lanthanum Ferrite, *J. Solid State Chem.*, 2007, **180**, 1489–1503.

28 J. Mizusaki, T. Sasamoto, W. R. Cannon and H. K. Bowen, Electronic Conductivity, Seebeck Coefficient, and Defect Structure of $La_{1-x}Sr_xFeO_3$ ($x = 0.1$, 0.25), *J. Am. Ceram. Soc.*, 1983, **66**, 247–252.

29 Z. C. Shen, *et al.*, Increased Activity in the Oxygen Evolution Reaction by Fe^{4+}-Induced Hole States in Perovskite $La_{1-x}Sr_xFeO_3$, *J. Mater. Chem. A*, 2020, **8**, 4407–4415.

30 N. P. Brandon, S. Skinner and B. C. H. Steele, Recent Advances in Materials for Fuel Cells, *Annu. Rev. Mater. Res.*, 2003, **33**, 183–213.

31 D. D. Taylor, N. J. Schreiber, B. D. Leyitas, W. Q. Xu, P. S. Whitfield and E. E. Rodriguez, Oxygen Storage Properties of $La_{1-x}Sr_xFeO_{3-\delta}$ for Chemical-Looping Reactions-an in Situ Neutron and Synchrotron X-Ray Study, *Chem. Mater.*, 2016, **28**, 3951–3960.

32 S. E. Dann, D. B. Currie, M. T. Weller, M. F. Thomas and A. D. Alrawwas, The Effect of Oxygen Stoichiometry on Phase Relations and Structure in the System $La_{1-x}Sr_xFeO_{3-\delta}$ ($0 \leq x \leq 1$, $0 \leq \delta \leq 0.5$), *J. Solid State Chem.*, 1994, **109**, 134–144.

33 H. Falcon, J. A. Barbero, J. A. Alonso, M. J. Martinez-Lope and J. L. G. Fierro, $SrFeO_{3-\delta}$ Perovskite Oxides: Chemical Features and Performance for Methane Combustion, *Chem. Mater.*, 2002, **14**, 2325–2333.

34 A. D. Al-Rawwas, C. E. Johnson, M. F. Thomas, S. E. Dann and M. T. Weiler, Mössbauer Studies on the Series $La_{1-x}Sr_xFeO_3$, *Hyperfine Interact.*, 1994, **93**, 1521–1529.

35 H. Y. Chong, S. H. Lee and T. W. Kim, Effect of an Ultraviolet-Ozone Treatment on the Electrical Properties of Titanium-Oxide Thin-Film Transistors Fabricated by Using a Sol-Gel Process, *J. Electrochem. Soc.*, 2012, **159**, B771–B774.

36 A. Klasen, *et al.*, Removal of Surface Oxygen Vacancies Increases Conductance through TiO_2 Thin Films for Perovskite Solar Cells, *J. Phys. Chem. C*, 2019, **123**, 13458–13466.

37 X. Luo, T. Su, X. Xie, Z. Qin and H. Ji, The Adsorption of Ozone on the Solid Catalyst Surface and the Catalytic Reaction Mechanism for Organic Components, *ChemistrySelect*, 2020, **5**, 15092–15116.

38 J. I. Jung, M. Risch, S. Park, M. G. Kim, G. Nam, H. Y. Jeong, Y. Shao-Horn and J. Cho, Optimizing Nanoparticle Perovskite for Bifunctional Oxygen Electrocatalysis, *Energy Environ. Sci.*, 2016, **9**, 176–183.

39 H. M. Rietveld, A Profile Refinement Method for Nuclear and Magnetic Structures, *J. Appl. Crystallogr.*, 1969, **2**, 65–71.
40 J. Rodriguez-Carvajal, Recent Advances in Magnetic Structure Determination by Neutron Powder Diffraction, *Phys. B*, 1993, **192**, 55–69.
41 A. Vaitkus, A. Merkys and S. Grazulis, Validation of the Crystallography Open Database Using the Crystallographic Information Framework, *J. Appl. Crystallogr.*, 2021, **54**, 661–672.
42 M. Quiros, S. Grazulis, S. Girdzijauskaite, A. Merkys and A. Vaitkus, Using SMILES Strings for the Description of Chemical Connectivity in the Crystallography Open Database, *J. Cheminf.*, 2018, **10**, 23.
43 A. Merkys, A. Vaitkus, J. Butkus, M. Okulic-Kazarinas, V. Kairys and S. Grazulis, COD::CIF::Parser: An Error-Correcting CIF Parser for the Perl Language, *J. Appl. Crystallogr.*, 2016, **49**, 292–301.
44 S. Grazulis, A. Merkys, A. Vaitkus and M. Okulic-Kazarinas, Computing Stoichiometric Molecular Composition from Crystal Structures, *J. Appl. Crystallogr.*, 2015, **48**, 85–91.
45 S. Grazulis, A. Daskevic, A. Merkys, D. Chateigner, L. Lutterotti, M. Quiros, N. R. Serebryanaya, P. Moeck, R. T. Downs and A. Le Bail, Crystallography Open Database (COD): An Open-Access Collection of Crystal Structures and Platform for World-Wide Collaboration, *Nucleic Acids Res.*, 2012, **40**, D420–D427.
46 S. Grazulis, D. Chateigner, R. T. Downs, A. F. T. Yokochi, M. Quiros, L. Lutterotti, E. Manakova, J. Butkus, P. Moeck and A. Le Bail, Crystallography Open Database - an Open-Access Collection of Crystal Structures, *J. Appl. Crystallogr.*, 2009, **42**, 726–729.
47 R. T. Downs and M. Hall-Wallace, The American Mineralogist Crystal Structure Database, *Am. Mineral.*, 2003, **88**, 247–250.
48 C. Haavik, T. Atake and S. Stolen, On the Enthalpic Contribution to the Redox Energetics of $SrFeO_{3-\delta}$, *Phys. Chem. Chem. Phys.*, 2002, **4**, 1082–1087.
49 O. Haas, U. F. Vogt, C. Soltmann, A. Braun, W. S. Yoon, X. Q. Yang and T. Graule, The Fe K-Edge X-Ray Absorption Characteristics of $La_{1-x}Sr_xFeO_{3-\delta}$ Prepared by Solid State Reaction, *Mater. Res. Bull.*, 2009, **44**, 1397–1404.
50 O. Clemens, M. Kuhn and R. Haberkorn, Synthesis and Characterization of the $La_{1-x}Sr_xFeO_{3-\delta}$ System and the Fluorinated Phases $La_{1-x}Sr_xFeO_{3-x}F_x$, *J. Solid State Chem.*, 2011, **184**, 2870–2876.
51 M. Kuhn, S. Hashimoto, K. Sato, K. Yashiro and J. Mizusaki, Oxygen Nonstoichiometry, Thermo-Chemical Stability and Lattice Expansion of $La_{0.6}Sr_{0.4}FeO_{3-\delta}$, *Solid State Ionics*, 2011, **195**, 7–15.
52 C. H. Wei, F. Z. Zhang, Y. Hu, C. H. Feng and H. Z. Wu, Ozonation in Water Treatment: The Generation, Basic Properties of Ozone and Its Practical Application, *Rev. Chem. Eng.*, 2017, **33**, 49–89.
53 Y. J. Xie, M. D. Scafetta, E. J. Moon, A. L. Krick, R. J. Sichel-Tissot and S. J. May, Electronic Phase Diagram of Epitaxial $La_{1-x}Sr_xFeO_3$ Films, *Appl. Phys. Lett.*, 2014, **105**, 062110.
54 Y. J. Xie, M. D. Scafetta, R. J. Sichel-Tissot, E. J. Moon, R. C. Devlin, H. Q. Wu, A. L. Krick and S. J. May, Control of Functional Responses Via Reversible Oxygen Loss in $La_{1-x}Sr_xFeO_{3-\delta}$ Films, *Adv. Mater.*, 2014, **26**, 1434–1438.
55 H. Yamada, M. Kawasaki and Y. Tokura, Epitaxial Growth and Valence Control of Strained Perovskite $SrFeO_3$ Films, *Appl. Phys. Lett.*, 2002, **80**, 622–624.